10-2014

Passive Phase Separation of Microgravity Bubbly Flows Using Conduit Geometry

Ryan M. Jenson
IRPI

Andrew Paul Wollman
Portland State University

Mark M. Weislogel
Portland State University, weisloge@pdx.edu

Lauren Sharp
NASA Glenn Research Center

Robert Green
NASA Glenn Research Center

See next page for additional authors

Citation Details

Jenson, R. M., Wollman, A. P., Weislogel, M. M., Sharp, L., Green, R., Canfield, P. J., & ... Dreyer, M. E. (2014). Passive phase separation of microgravity bubbly flows using conduit geometry. International Journal Of Multiphase Flow, 6568-81.

International Journal of Multiphase Flow 65 (2014) 68–81

Contents lists available at ScienceDirect

International Journal of Multiphase Flow

journal homepage: www.elsevier.com/locate/ijmulflow

Passive phase separation of microgravity bubbly flows using conduit geometry

Ryan M. Jenson [a], Andrew P. Wollman [b], Mark M. Weislogel [b,*], Lauren Sharp [c], Robert Green [c], Peter J. Canfield [d], Jörg Klatte [d], Michael E. Dreyer [d]

[a] IRPI, LLC, 7929 SW Burns Way STE A, Wilsonville, OR 97070, United States
[b] Portland State University, Dept. Mechanical and Materials Engineering, 1930 SW 4th Avenue, Portland Oregon, 97201, United States
[c] NASA Glenn Research Center, 21000 Brookpark Road, Cleveland, OH 44135, United States
[d] Center of Applied Space Technology and Microgravity, Am Fallturm ZARM-II, 1550, 28359 Bremen, Germany

ARTICLE INFO

Article history:
Received 5 February 2014
Received in revised form 14 May 2014
Accepted 17 May 2014
Available online 6 June 2014

Keywords:
Two-phase flow
Capillary fluidics
Microfluidics
Passive phase separations
Microgravity
Spacecraft

ABSTRACT

The ability to separate liquid and gas phases in the absence of a gravitational acceleration has proven a challenge to engineers since the inception of space exploration. Due to our singular experience with terrestrial systems, artificial body forces are often imparted in multiphase fluid systems aboard spacecraft to reproduce the buoyancy effect. This approach tends to be inefficient, adding complexity, resources, and failure modes. Ever present in multiphase phenomena, the forces of surface tension can be exploited to aid passive phase separations where performance characteristics are determined solely by geometric design and system wettability. Said systems may be readily designed as demonstrated herein where a regulated bubbly flow is drawn through an open triangular sectioned duct. The bubbles passively migrate toward the free surface where they coalesce and leave the flow. The tests clearly show container aspect ratios required for passive phase separations for various liquid and gas flow rates. Preliminary data are presented as regime maps demarking complete phase separation. Long duration microgravity experiments are performed aboard the International Space Station. Supplementary experiments are conducted using a drop tower.

1. Introduction

Separation of bubbles from a liquid medium is a critical, but non-trivial task aboard spacecraft due to the absence of a net gravitational force that precludes using buoyancy as a strong separation mechanism. Without gravity-induced buoyancy, alternate methods such as artificial body forces must be utilized to achieve partial or complete phase separation. Artificial accelerations may be imparted by onboard centrifuges (Ozbolt, 1996), thruster firings (Chato and Martin, 2006), or by designing vortical flow paths in pumped loops (Chahine and Kalumuck, 2001; Barbu et al., 2006; Hoyt et al., 2011). Body or surface forces generated by electric, magnetic, acoustic, and other forces are also considerable (Feng and Seyed-Yagoobi, 2004; Marchetta et al., 2004; Oeftering et al., 2002; Clark, 1992; Shoemaker and Schrage, 1997), but no approach has been met with wide acceptance and implementation. This is primarily the result of the extremely limited exposure to long duration low-*g* environments where a sense of routine is difficult to establish and where inferior methods are only slowly removed from consideration.

An additional and ever-present force in spacecraft fluids systems is the capillary force which exploits the combination of surface tension, wetting characteristics, and system geometry as the primary mechanism for fluid control, including phase separations. In ideal situations, a 'capillary solution' can provide the driving force for the flow as well as all fluids management operations including phase separation and recirculation. The modern heat pipe provides an ideal case in point (Ku, 1999). At the other end of the spectrum, capillary forces may be perceived as an annoyance and design workarounds may be considered rendering the system 'capillary-free' and therefore ground-testable. An excellent example of this approach is the single phase liquid cooling loop of the International Space Station (ISS) (Thurman and McCall, 1992). But the capillary force is unavoidable when fluid interfaces are present and experience to date suggests their likelihood is inevitable, as discovered for the same ISS cooling loop where gas leaks into the system over time create an inadvertent two-phase system (Orlando and Ferrara, 1992). Even systems

* Corresponding author. Tel.: +1 5037254292.
E-mail address: mwei@pdx.edu (M.M. Weislogel).

http://dx.doi.org/10.1016/j.ijmultiphaseflow.2014.05.011
0301-9322/

designed with non-capillary solutions should consider capillarity at all levels to enhance the reliability of the overall system.

For spacecraft, we consider every sub-system such as a condenser, evaporator, or packed bed, and every sub-element, such as a valve, fitting, filter, accumulator, or manifold as a potential multiphase flow generator or separator. By careful selection of component geometry one might distribute passive phase separation, collection, and control operations throughout the system, greatly improving reliability—even if the system is not considering capillarity as the central motive force for the flow or flow separation function. In this paper we consider a wedge geometry that provides a passive capillary means for separating gas bubbles from a liquid flow. With special consideration for applications in low-g environments, the simple flow mechanism is briefly reviewed via drop tower experiments and an expedient scale analysis. A description of ISS space experiments is then provided along with a narrative of the experimental procedure, breadth of experiments conducted, and follow-on tests planned. Sample images of the flight data are provided along with reduced data presented as regime maps for the tests completed to date. Much is learned from simple inspection of the data, but the foundational message here is the ease with which certain two-phase flows may be passively separated using a simple asymmetric conduit.

2. Mechanism for low-g bubble migration in a wedge

In the microgravity environment buoyancy forces are often negligible and in the absence of significant imposed inertial forces, fluid interfacial configurations are determined entirely by capillary forces. The relative strength of body forces to surface tension forces is characterized by the Bond number $Bo = \Delta\rho a R^2/\sigma$, where $\Delta\rho$ is the density difference between the two fluid phases, a is the local acceleration often represented by compensated gravity g, R is a characteristic surface length scale, and σ is the surface tension. When $Bo \ll 1$, surface forces overpower gravity and capillary fluidic phenomena predominate. Such conditions occur over small length scales in a terrestrial environment, but over unusually large length scales in a microgravity environment.

A confined bubble in a narrow wedge consisting of two plane walls filled with a quiescent liquid is sketched in Fig. 1. Body forces are neglected; i.e., $Bo \ll 1$. For a known bubble volume V_b, lengths R_1, R_2, and R_3 provide characterizations of the various radii of curvature of the bubble surface. The local interface curvature is highest at the narrower side of the bubble ($\sim -1/R_1$ to $1/R_3$) and the liquid pressure is lowest there (Fig. 1c). Increasingly higher pressure liquid toward the wider side of the bubble ($\sim -1/R_2$ to $1/R_3$) flows circumferentially around the bubble to the narrower side displacing the bubble away from the vertex until it is at least fully inscribed within the wedge cross section. In terms of the driving pressure difference, the impact of the $1/R_3$ curvature approximately cancels.

Metz et al. (2010) and Reyssat (2014) study confined bubble migration analytically assuming a wetting quiescent liquid. Reyssat adds useful solutions for similarly migrating wetting drops, which travel in the opposite direction toward the vertex. It is not difficult to imagine how such conduit geometries might be exploited to provide a passive means of bubble manipulation in terrestrial microfluidics systems (Zhao et al., 2001; Melin et al., 2005; Skelleya and Voldmana, 2008; Xu et al., 2010) as well as systems in the near weightless environment of orbiting spacecraft (Jaekle, 1991; Chato and Martin, 2006; Weislogel et al., 2009; Pettit et al., 2011). In keeping with an example of the latter, a liquid bearing enclosure with an acute isosceles triangular cross section is presented in Fig. 2. A gas bubble of known volume is introduced into the wetting liquid. The highly acute vertex points upwards such that under normal gravity conditions the confined gas bubble elongates along the z-axis with a capillary height $H_b \sim (\sigma/\rho g)^{1/2}$. Provided the Concus–Finn wetting condition $\theta < \pi/2 - \alpha$ is satisfied, where θ is the contact angle and α is the acute vertex half-angle (Concus and Finn, 1969), upon step reduction of gravity as occurs during a typical drop tower test, corner flows wick further into and along the corner by well-established means displacing the bubble away from the vertex (see Weislogel et al. (2011) and references cited therein). The predominately 1-D corner flow mechanism gives way quickly to a 2-D disc-like flow prior to an eventual more 3-D flow as the bubble becomes increasingly spherical, ultimately coming to rest to various degrees inscribed by the container cross section. The dynamics of this process are sketched in perspective in Fig. 2a with a sample drop tower experiment shown in profile in Fig. 2b. The drop tower experiment is performed for a 40 μl air bubble in a 52 mm long, 16.5 mm tall acrylic container with vertex half-angle $\alpha = 7.75°$ in perfectly wetting 5 cSt polydimethylsiloxane (PDMS).

To clarify the bubble separation characteristics of this geometry, a similar acute wedge-sectioned conduit is sketched in Fig. 3 oriented again such that the highly acute vertex points upward. In this case the conduit is open along the lower face where a free surface serves as a stable containing surface for the flow. Terrestrial demonstrations of such a flow are possible provided $Bo \leqslant 2.74$ (Concus, 1964). For a similar experiment to the drop tower test shown in Fig. 2, the confined gas bubble of Fig. 3a passively migrates downward in the initially quiescent liquid, and, being large enough not to fully inscribe within the section before the free surface is reached, the bubble is forced against the free surface where it coalesces and leaves the liquid. In the case of Fig. 3b, when the liquid is driven left to right through such a conduit by a pump (a 'non-zero' base state liquid flow) bubbles emanating from the upstream vertex region are swept downstream while they simultaneously migrate away from the vertex as described in Figs. 1–3a. Provided the bubble volume is large enough and the liquid flow rate is low enough, the bubbles reach the free surface within the available duct length L, where they coalesce and leave the liquid stream. What is of interest for the purposes of design in such cases might be the length l of the open conduit section required to collect the bubbles for various liquid–gas flow rate ratios, bubble size and frequency, conduit size, geometry, and fluid properties. Experimentation in the low-g environment provides a rare opportunity to investigate such buoyancy-free, large length scale, inertial-capillary flows that often only occur therein.

3. Bubble migration with and without base liquid flow

3.1. Scales for zero base flow

Due to the many variables of the flow and the experimental nature of this presentation, a scale analysis is quickly performed such that useful dimensionless groups might be identified providing a basis for comparisons of terrestrial, drop tower, and space flight experiments. A more thorough analytical and numerical analysis of the fluid mechanics of the problem is also underway and will be reported separately.

Referring to Fig. 1, the steady x-component momentum equation $\rho(\bar{u}\cdot\nabla)u = -P_x + \mu\nabla^2 u$, where $\bar{u} = (u, v, w) \sim U$, may be written as the characteristic x-velocity scale equation

$$\frac{\rho U^2}{2L_s} \sim \frac{\sigma}{R_s L_s}, \frac{\mu U}{y_s^2} \tag{1}$$

where L_s, R_s, and y_s are characteristic scale lengths for the flow, capillary radius of curvature, and viscous resistance, respectively. Employing the length dimensions identified in Fig. 1, and for brevity

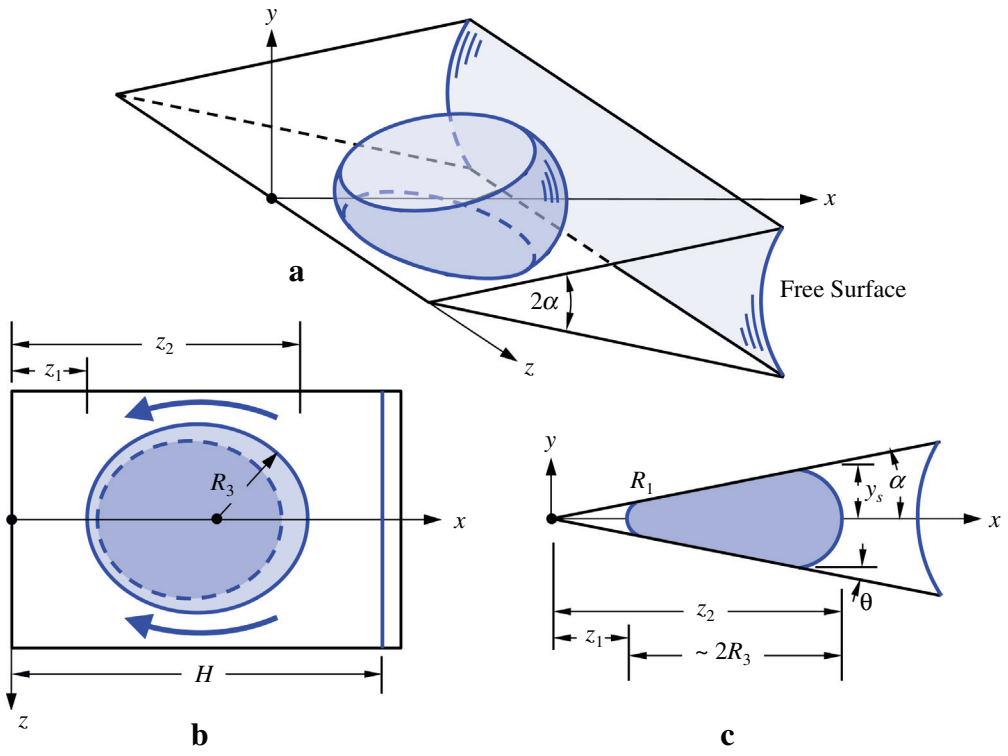

Fig. 1. Schematic of confined bubble migration in a wedge with zero-velocity liquid base state (quiescent liquid): (a) isometric view, (b) top view, and (c) profile view. R_3 characterizes the radius of curvature in the x–z plane while R_1 and R_2 characterize local radii of curvature in the x–y plane. The leftward arrows in (b) indicate the liquid flow direction largely resulting in the displacement of the bubble rightward. Depending on the wettability and speed of the bubble migration, thin liquid films may exist between the bubble and the planar walls. Such layers are not shown in c., though they are always present in the experiments reported herein due to the choice of perfectly wetting liquids.

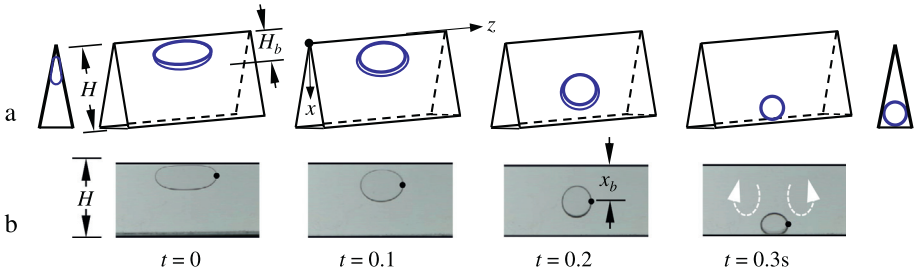

Fig. 2. (a) Schematic perspective view for a time sequence of spontaneous bubble migration out of the interior corner of an acute triangular enclosure upon step reduction in gravity level during a typical drop tower test. (b) Dynamic bubble profile imaged at times identified for a 40 μl air bubble in perfectly wetting 5 cSt PDMS, and an enclosure with vertex half-angle $\alpha = 7.75°$. The leading bubble meniscus location $x_b(t)$ is identified with a dot and residual wake vortical flows for $Su^+ \gg 1$ are sketched using dashed lines at the lower right. At $t = 0.3$ s the bubble remains confined, pressed against the lower surface of the enclosure by capillary forces.

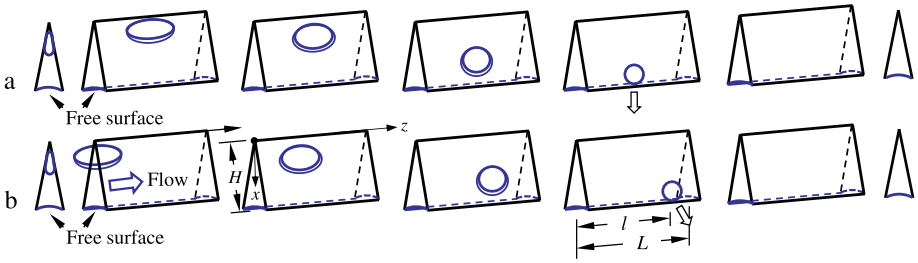

Fig. 3. (a) Time series of low-g capillary-dominated bubble migration in the presence of a free surface in an acute wedge-sectioned conduit of length L (zero base flow). If the bubble is large enough, it is forced against the free surface where it coalesces and leaves the conduit. (b) The similar process as in (a), but superimposed on a forced liquid flow through the duct (non-zero base flow). The bubble is swept downstream as it migrates away from the vertex leaving the conduit through the free surface a distance l from its initial location.

here, assuming $z_1 \ll z_2$, $\tan\alpha \ll 1$, and $\theta \ll 1$, by choosing $R_s \sim y_s \sim z_2 \tan\alpha$ and $L_s \sim z_2$, where $z_2 \sim (V_b/\tan\alpha)^{1/3}$, Eq. (1) may be solved algebraically for the characteristic x-component bubble migration velocity $U \sim U_b$ from

$$\frac{\rho U_b^2}{2L_s} + \frac{\mu U_b}{y_s^2} - \frac{\sigma}{R_s L_s} \approx 0.$$

The physically meaningful root is

$$U_b = \frac{1}{Su^+}\left(\frac{\sigma y_s^2}{\mu L_s R_s}\right)\left((1+2Su^+)^{1/2} - 1\right), \tag{2}$$

where, under the above length scale restrictions,

$$Su^+ \equiv Su \cdot \frac{y_s^3}{R_s L_s^2} \equiv \left(\frac{\rho\sigma y_s}{\mu^2}\right) \cdot \frac{y_s^3}{R_s L_s^2} \sim \frac{\rho\sigma}{\mu^2} V_b^{1/3} \tan^{8/3}\alpha.$$

Su is the Suratman number—a so-called capillary Reynolds number—measuring the strength of inertial to viscous resistance in an otherwise capillarity-driven flow. From Eq. (2), for visco-capillary flows $Su^+ \ll 1$, and Eq. (2) reduces to

$$U_b = \frac{\sigma y_s^2}{\mu L_s R_s} = \frac{\sigma}{\mu}\tan\alpha. \tag{3}$$

For inertial-capillary flows $Su^+ \gg 1$, and Eq. (2) reduces to

$$U_b = \left(\frac{2\sigma}{\rho R_s}\right)^{1/2} = \left(\frac{2\sigma}{\rho V_b^{1/3}\tan^{2/3}\alpha}\right)^{1/2}. \tag{4}$$

Eqs. (3) and (4) provide characteristic *steady* velocities for the bubble motion away from the corner in a host fluid which is our short term analytical goal. In the narrow wedge limit, and with broader regard for the changing length scales of the problem, Reyssat (2014) identifies the viscous scaling of Eq. (3), but also an additional scale when $z_1 \sim z_2$, which addresses an intermediate time- and volume-dependent regime dominated by losses at moving contact lines, where $U_b \sim \left(\sigma V_b^{3/4}/\mu\right)^{4/13} t^{-9/13}$. For both visco- and inertial-capillary flows, further complexities are expected for various initial conditions, increasingly spherical bubbles, large wedge angles, large bubble volumes, liquid films, increasingly inertial flows, and others, but the regimes of Eqs. (3) and (4) are treated here as preliminary design guides.

3.2. Drop tower experiments

Select transient results of bubble migration experiments conducted using a 2.1 s drop tower are provided in Fig. 4a, with representative images provided in Fig. 2b. In Fig. 4 only the leading bubble meniscus locations (x_b, Fig. 2b) are plotted in time for clarity. Details of the drop tower employed may be found in Wollman (2012) and nominal thermophysical properties and important dimensionless parameters are listed in Appendix A. In Fig. 4a, and for brevity here, a limited variety of viscous PDMS fluids are shown along with tests using fluid HFE-7500 for a fixed wedge half-angle $\alpha = 7.75°$. Hash marks are used to indicate x-coordinate bubble center elevations defined as x_i, where an assumed spherical bubble of volume V_b is first inscribed within the planar walls of the wedge section. For the initially quiescent liquid drop tower tests, the bubbles in the under-damped low viscosity HFE-7500 fluid ($Su^+ \sim 200$) clearly overshoot their inscribed elevations, whereas the bubbles in the over-damped high viscosity PDMS liquids ($Su^+ \sim 0.1$) approach such elevations gradually from below. The overshoot concerning the former is significant and appears to be driven by vortical flows induced in the liquid whose inertia continues to carry the bubbles beyond the inscribed location x_i as sketched in Fig. 2b. Such recirculation cells are observed by Metz et al. (2010) as well. In Fig. 4a, for the inertial HFE-7500 tests a common initial capillary migration velocity is observed that is weakly, if not at all, dependent on bubble volume (from Eq. (4), $U_b \sim V_b^{1/6}$). In Fig. 4b, select tests using HFE-7500 are compared to similar data collected from bubble injections during the Capillary Channel Flow (CCF) spaceflight experiments with non-zero base liquid flows and $\alpha = 7.9°$, which will be described shortly. The common initial migration velocity is maintained for both zero and non-zero base state flows, and semi-quantitative agreement in Eq. (4) is approximated by $U_b \approx 0.334\ (2\sigma/\rho V_b^{1/3}\tan^{2/3}\alpha)^{1/2} \approx 0.0375$ m/s. At present, viscous dominated behavior from Eq. (3) is roughly approximated by $U_b \approx 0.03(\sigma/\mu)\ \tan\alpha \approx 0.002$ m/s despite the clear but weak bubble volume dependence observed in Fig. 4a. A wealth of both drop tower and microscale terrestrial data have been collected along these lines and is expected to be presented along with a formal analysis in a subsequent publication.

3.3. Scales for non-zero base flow

Observations from Fig. 4b suggest that inertial bubble migrations with $Su^+ \gg 1$ appear to possess a common initial

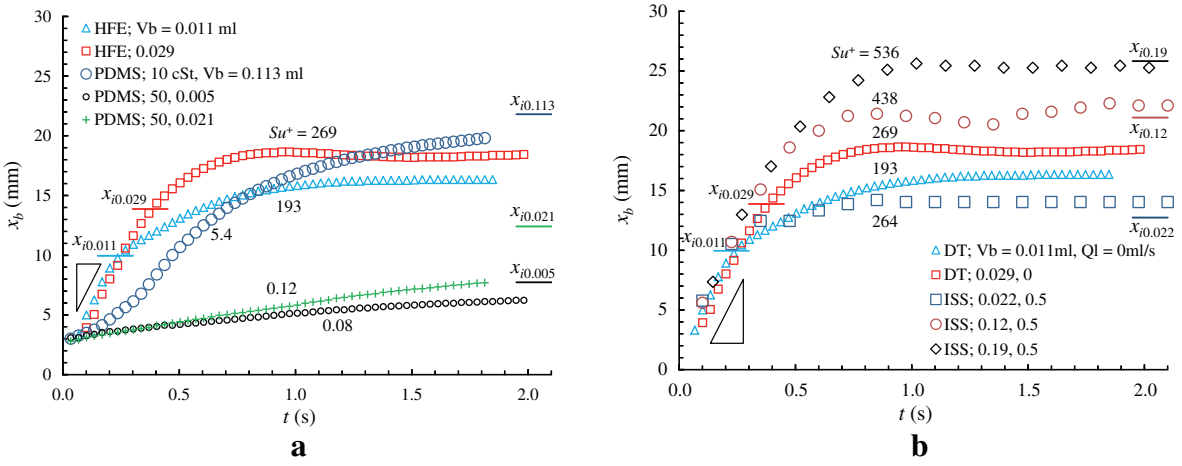

Fig. 4. Select leading meniscus bubble elevations $x_b(t)$ for (a) drop tower tests with in quiescent liquid and (b) said drop tower tests compared to CCF ISS space experiment data with non-zero liquid base flow for HFE-7500 fluid only. In (a) the fluid viscosity varies between under-damped and over-damped states as indicated by the value of Su^+ and by the over/under-shoot of the ideal inscribed spherical bubble elevations identified by the x_{iVb} tick marks. Here, $Su^+ = (\rho\sigma V_b^{1/3}/\mu^2)\tan^{8/3}\alpha$. The common slope for the large Su^+ tests is identified by the triangle where $U_b = 37.5$ mm/s. Note also that $H \geqslant 30$ mm for all of the wedge vessels tested.

migration velocity that is fairly independent of bubble volume and base liquid flow condition and that a base flow dramatically reduces the impact of the inscribed elevation overshoot mechanism described above, observed in Fig. 4 for the HFE-7500 fluid, and sketched generically in Fig. 2b. Thus, when forced convective liquid flows are present the bubbles achieve elevations near to the inscribed conditions x_i as shown in Fig. 4b. This observation serves as a guide to the design of systems expecting to exploit such phenomena for passive fluid control. The weak dependence of the bubble migration velocity on the base flow adds credibility to an argument for the superposition of the migration rate and the liquid velocity profile to estimate bubble paths ultimately leading to characteristic channel length predictions for bubble separation as is attempted in this section.

Treating the bubble as a particle, the bubble velocity may be approximated vectorially as $\bar{u} = (u, v, w) \approx (u, 0, w) \sim (U_b, 0, w)$. The x-component $u \sim U_b$ may be estimated from Eqs. (2)–(4). Any y-averaged streamwise velocity profile might then be invoked to serve as an x-dependent z-component of velocity $\langle w \rangle$. As a preliminary demonstration, three such profiles are employed here to generate quick guides for system design: fully developed, linear, and plug forced liquid velocity profiles. The primary objective of this exercise is to develop an estimate for bubble exit length l for the extremes in conditions possible in the wedge conduit geometry.

For a narrow corner half-angle $\alpha \ll 1$, it may be shown for a fully developed forced flow along an open wedge conduit (Weislogel and Lichter, 1998) that average z-component velocities $\langle w \rangle$ in y–z-planes may be expressed as

$$\langle w \rangle = -\frac{P_z x^2 \sin^2 \alpha}{3\mu \cos 2\alpha}, \tag{5}$$

where P_z is the imposed pressure gradient along the open triangular duct. Steady x-component bubble velocities such as Eqs. (2)–(4) may be substituted into Eq. (5) to parameterize w in terms of time where $x = U_b t + x_o$. The time-dependent z-axis bubble location $l(t)$ may then be determined via

$$l(t) = \int_0^t \langle w \rangle d\hat{t} = -\frac{P_z \sin^2 \alpha}{9U_b \mu \cos 2\alpha}\left[(U_b t + x_o)^3 - x_o^3\right]. \tag{6}$$

Evaluated at the free surface where $t_H = (H - x_o)/U_b$, Eq. (6) gives

$$l(t_H) = -\frac{P_z H^3 \sin^2 \alpha}{9\mu U_b \cos 2\alpha}\left[1 - \left(\frac{x_o}{H}\right)^3\right]. \tag{7}$$

The flow rate may be determined by integrating Eq. (5) over the section area to find $Q_l = \int \langle w \rangle dA = \int_0^H \langle w \rangle 2x \tan \alpha dx = -P_z H^4 \sin^2 \alpha \tan \alpha/(6\mu \cos 2\alpha)$, from which P_z may be written in terms of Q_l. Substituting this relationship into Eq. (7) yields,

$$l(t_H) = \frac{2Q_l}{3U_b H \tan \alpha}\left[1 - \left(\frac{x_o}{H}\right)^3\right], \tag{8}$$

which serves as a characteristic length within which bubbles might be expected to migrate to the free surface, coalesce, and leave the flow.

Experimental observations suggest that linear profiles may be present at moderate to high liquid flow rates in developing flows. A model for such flow might assume

$$\langle w \rangle = -\frac{C_1 P_z x \tan \alpha}{\mu}, \tag{9}$$

from which it is found that

$$l(t_H) = \frac{3Q_l}{4U_b H \tan \alpha}\left[1 - \left(\frac{x_o}{H}\right)^2\right]. \tag{10}$$

At even higher flow rates, a uniform plug flow might be expected where

$$\langle w \rangle = \frac{Q_l}{H^2 \tan \alpha}, \tag{11}$$

and

$$l(t_H) = \frac{Q_l}{U_b H \tan \alpha}\left[1 - \frac{x_o}{H}\right]. \tag{12}$$

From Eqs. (8), (10), and (12), for $x_o/H \ll 1$, $l(t_H) \equiv l_H \sim Q_l/(U_b H \tan \alpha)$ regardless of the base state liquid velocity profile. Employing such relationships, Table 1 summarizes the scaling results for U_b, l_H, and t_H for respective visco- and inertial-capillary bubble migration, where t_H is the characteristic time required for the bubble to first reach the free surface a distance $l(t)$ downstream from the initial bubble location. Dimensions including l and H are identified in Fig. 3b. The experiments employing HFE-7500 achieve $Su^+ \sim O(100)$ for the bubble migration while the forced free stream flows, to be introduced shortly, are laminar with $Re \sim O(100)$. Under such conditions inertial-capillary bubble migrations within developing laminar forced conduit flows are expected. In this case, Table 1 figure of merit is l_H for $Su^+ \gg 1$ which is only weakly dependent on bubble volume $\sim V_b^{1/6}$.

4. The capillary channel flow experiment aboard ISS

The Capillary Channel Flow (CCF) experiment is a fully remote controlled space flight experiment that was conceived at the ZARM scientific institute of the University of Bremen, designed and built by Astrium (an EADS company), and flown to the ISS by NASA on the Space Shuttle STS 131, 5 April, 2010. The hardware development is funded by the German Aerospace Center (DLR) while integration, launch and flight operations are funded by NASA. To operate CCF on ISS the hardware must be installed in the Microgravity Science Glovebox by an astronaut (MSG, Spivey et al., 2008). The equipment is then connected for remote commanding from ground stations in Germany and the USA. The experiment can operate without interruption for months and to date three operations have been completed providing over 140 days of continuous run time.

The CCF experiment primarily focuses on the investigation of steady limiting flow rates in open channel inertial-capillary flows in the long-term microgravity environment of the ISS. Though not the subject of this paper, these single-phase flow rate limitations have been explored in general by Rosendahl et al. (2004) and Rosendahl and Dreyer (2007) and specifically for the wedge section by Klatte et al. (2008) and Klatte (2011). Representative results as well as a detailed description of the CCF flight experiment components and performance characteristics are addressed by Canfield et al. (2013). It is thoroughly demonstrated that the liquid flow rate through such open ducts is limited by a choking mechanism caused by an excessive under-pressure that develops in the liquid leading to gas ingestion at the interface nearest the liquid exit. This phenomenon is shown in Fig. 5 for the open wedge conduit at two slider positions; i.e., two free surface lengths L. In the present study we are interested in the ability of open capillary channels to separate bubbly flows not generate them. Thus, our focus is on channel flows that are subcritical when compared to the choking or ingestion limit. For brevity, unless otherwise specified, all data to be presented will be for fixed channel length $L = 48$ mm, where the critical choking flow rate, here denoted as the liquid flow ingestion limit, $Q_{ling} = 2.69$ ml/s.

4.1. Overview of CCF experiment hardware and test procedure

The CCF hardware is complicated by subsystems required to enable remote commanding of the experiment. The Optical

Table 1
Summary of scale quantities for $x_o/H \ll 1$, $l_H \approx Q_l/(U_b H \tan\alpha)$, and $Su^+ \equiv (\rho\sigma\, {V_b}^{1/3}/\mu^2)\tan^{8/3}\alpha$. Coefficients determined from experiments performed herein provide semi-quantitative relationships for use in preliminary design calculations. Note that bubbles must satisfy $V_b \gtrsim (4\pi/3)(H\sin\alpha/(1+\sin\alpha))^3$ to reach the free surface with the likelihood of escaping the flow.

Domain/quantity	U_b (m/s)	l_H (m)	t_H (s)
Viscous, $Su^+ \ll 1$	$0.03\frac{\sigma}{\mu}\tan\alpha$	$\frac{\mu Q_l}{0.03\sigma H\tan^2\alpha}$	$\frac{\mu H}{0.03\sigma\tan\alpha}$
Convective, $Su^+ \gg 1$	$0.334\left(\frac{2\sigma}{\rho V_b^{1/3}\tan^{2/3}\alpha}\right)^{1/2}$	$\frac{3.51}{0.334}\frac{Q_l}{H}\left(\frac{\rho V_b^{1/3}}{2\sigma\tan^{4/3}\alpha}\right)^{1/2}$	$\frac{H}{0.334}\left(\frac{\rho V_b^{1/3}\tan^{2/3}\alpha}{2\sigma}\right)^{1/2}$
Mixed mode, $Su^+ \sim 1$	Eq. (2)	$\frac{Q_l}{U_b H\tan\alpha}$	$\frac{H}{U_b}$

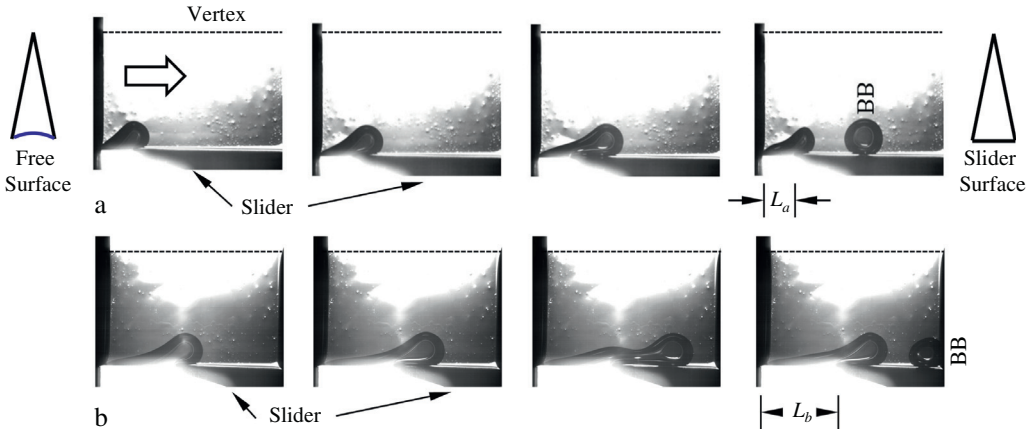

Fig. 5. Choking (ingestion limit) phenomenon in a wedge-sectioned conduit when pressure gradients in the pumped liquid exceed capillary pressure gradients at the free surface. (a) Section at left depicts free surface while section at right shows the closed conduit downstream. The wedge vertex is identified by the dashed line and BB identifies the first of many bubbles pinched off periodically by the instability. Images shown at 1.2 Hz during the CCF flight experiments aboard ISS are for base flow Q_{ling} = 3.93 ml/s in the direction identified by arrow with slider open length L_a = 10 mm (α = 7.9°, fluid HFE-7500, WE1433). (b) Images at 1.2 Hz for Q_{ling} = 3.65 ml/s with L_b = 20 mm (WE1291). For the majority of results presented herein, L = 48 mm, where Q_{ling} = 2.69 ml/s.

Diagnostic Unit (ODU), Electrical Subsystem (ESS), and an Experiment Unit (EU2) are identified in Fig. 6 which displays the hardware as installed in the MSG on ISS. The EU2 contains a variety of plungers, liquid and gas reservoirs, phase separation and liquid flow preparation chambers, valves, a pump, a flow meter, the test section containing the test channel, and numerous temperature, pressure, and conductivity sensors to manipulate and monitor the distribution of liquid and gas throughout the two-phase capillary system. A representative solid model of the EU2 is provided in Fig. 7 with key components identified. Further details of the transparent wedge channel test section are depicted schematically in Fig. 8 along with the optical elements. Only the functions of the open wedge test section (EU2) and essential plumbing in Fig. 9 will be described in detail. Refer to Canfield et al. (2013) for further information.

The illustration of Fig. 8 displays the open wedge channel with acute vertex upward. The transparent channel is L = 48 mm long,

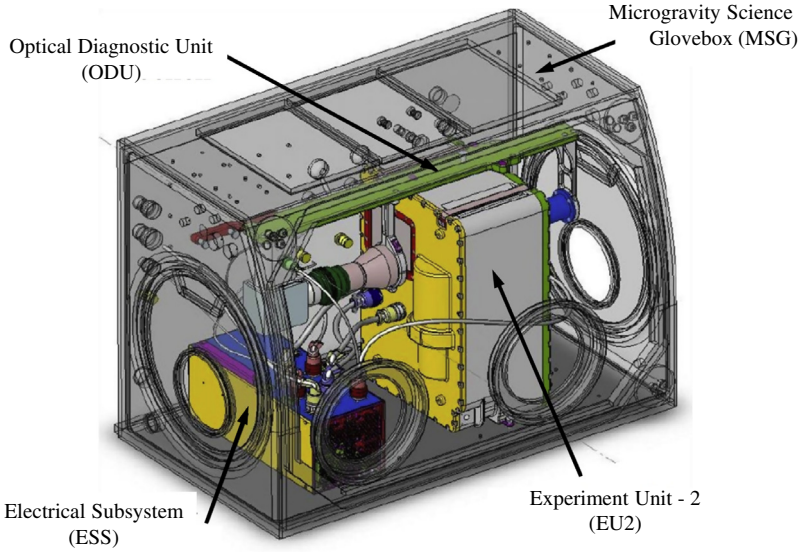

Fig. 6. Sketch of the CCF hardware as installed in the Microgravity Science Glovebox (MSG) aboard the International Space Station with key subsystems identified. The two MSG cameras are not shown.

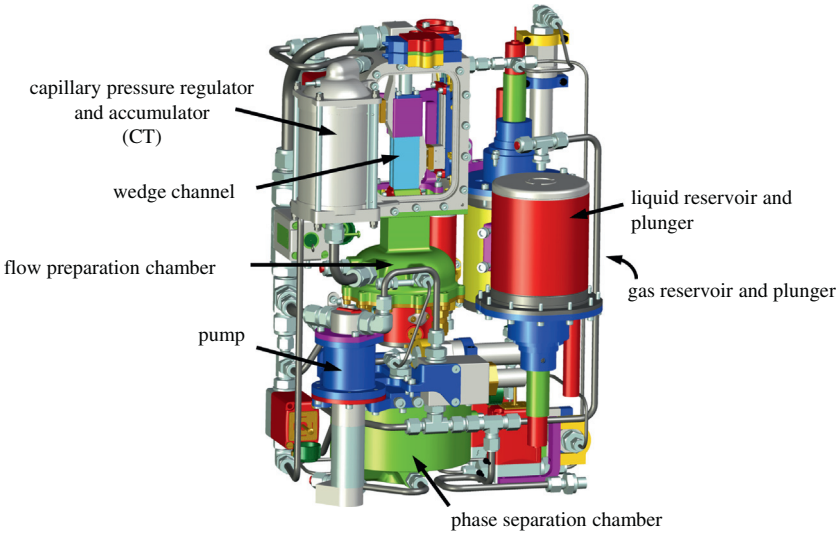

Fig. 7. Representative model of the internal components of the Experiment Unit (EU2) identified in Fig. 6.

$H = 30$ mm high at the vertex, with vertex half-angle $\alpha = 7.9°$. The translating slider shown in both Figs. 8 and 9 is used to vary the length of the free surface between 0 and 48 mm. The flow is drawn through the channel by a Micropump GB-P25 magnetic gear pump (0–20 ml/s) and the flow rate is determined by a Kobold DPM-1520-G2 flow meter (0.5–20 ml/s calibrated to ±0.1 ml/s such that $Q_l = 0.987 Q_{lpump} - 0.11$ ml/s with goodness of fit $\chi^2 = 0.999$). Bubbles are introduced into the channel through a cannula with 0.6/0.8 mm ID/OD. The cannula exit is located at the entrance of the transparent channel section with its centerline 3.6 mm distant from the channel vertex. As suggested in Fig. 9, gas bubbles are injected by use of a solenoid valve C2 via control of frequency $0 \leqslant f \leqslant 10$ Hz, duty cycle $0 \leqslant d \leqslant 10$ s, and gas supply conditions in the gas reservoir K3. There are at least three highly variable methods employed to generate bubbles: (1) bubble generator valve C2 wide open varying gas reservoir K3 pressure and/or K3 piston travel, (2) constant gas reservoir piston travel rate varying bubble valve C2 frequency and duty cycle, and (3) constant gas volume (constant K3 piston position) varying bubble valve C2 frequency and duty cycle. Only data recorded for the latter will be reported in detail here with approximate bubble volumes $0.004 \leqslant V_b \leqslant 2.14$ ml and typical frequencies of $0.2 \leqslant f \leqslant 2$ Hz achieved. Gas bubbles that pass through the test channel also pass through the pump and corrupt the flow meter before being filtered and captured in the Phase Separation Chamber (PSC, see Figs. 7 and 9). Each experiment is terminated before such bubbles reach the pump.

The gas injection procedure first develops a differential pressure of approximately 85 mbar between the approximately 356 ml gas reservoir K3 and the Flow Preparation Chamber (FPC). (The total upstream volume is comprised of K3, nominally 273 ml plus 78 ml K3 and 5 ml additional tubing dead volume). Average gas volumes upstream of the bubble valve C2 for K3 at 50% establish $V_1 \approx 220$ ml with average gas volumes downstream of C2 of $V_2 \approx 1110$ ml, the latter including all gas volumes in the PSC, CT, and EU2 enclosure. Next, the slider position and steady liquid flow conditions are established. The bubble injection valve C2 is then operated for any variety of frequencies and duty cycles provided the pressure in K3 does not drop below a differential pressure of 68 mbar. Thus the 'Constant Gas Volume Method' provides a 'constant gas supply pressure' to within ±10%. In the worst case, for the largest bubbles studied, this approach results in weakly diminishing bubble volumes during the bubble injection process—of less than 8% when the first bubble is considered, but less than 3% when the first bubble is not considered, the first bubble of a series being up to 5% larger in volume than subsequent bubbles. Though a decreasing bubble volume trend is expected and observed for the worst case largest bubbles, the majority of tests achieve standard

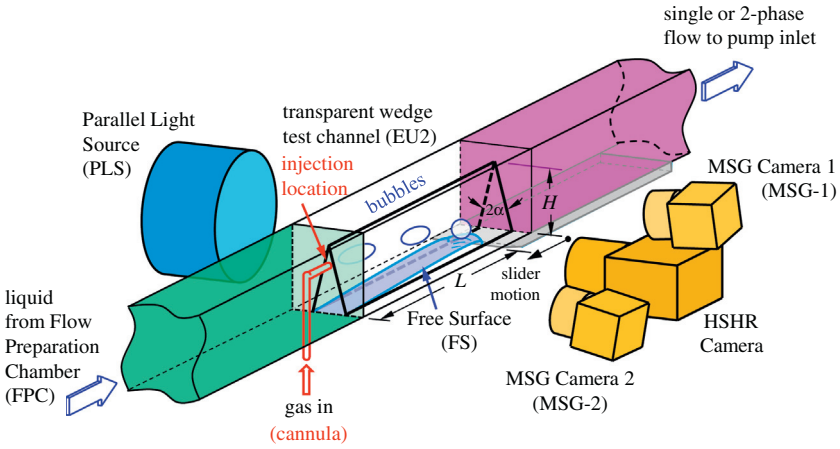

Fig. 8. Annotated schematic of the CCF-EU2 open wedge test channel with optical elements.

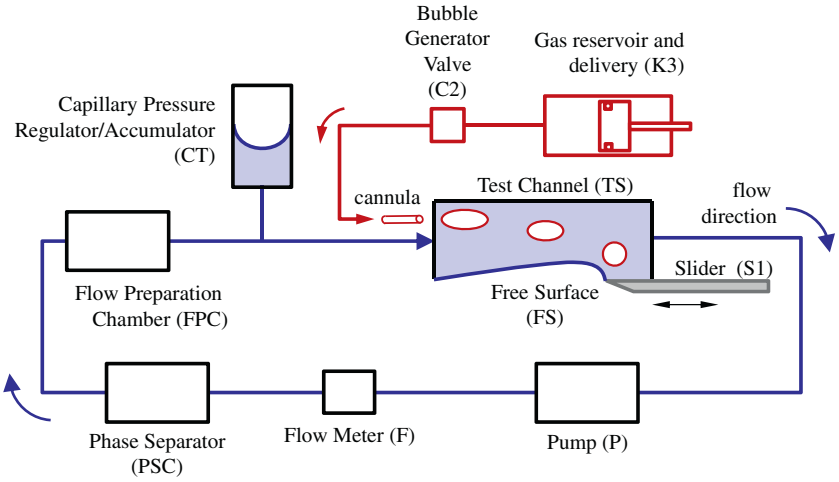

Fig. 9. Flow path of CCF-EU2 open wedge test channel with key plumbing and bubble injection elements. Abbreviations identified.

deviations in sequential bubble volumes of ±1%, which is below our measurement uncertainty limit.

As a guide to correlation development, the simplified model sketched in Fig. 10 for N_2, treated as an isothermal weakly compressible viscous ideal gas, is used to derive the dimensionless pressures

$$\frac{dP_1^*}{dt^*} = j^2 - 2\phi j P_1^* - (1-\phi^2)P_1^{*2} \tag{13}$$

and

$$P_2^* = j - \phi P_1^*, \tag{14}$$

subject to $P_1^*(t^*=0)=1$. The pressures are nondimensionalized by $P_{1i} \equiv P_1(0)$ such that $P_1^* = P_1/P_{1i}$ and $P_2^* = P_2/P_{1i}$ and

$$j \equiv \Omega + \phi; \quad k \equiv \frac{1-\Omega}{1+\Omega}; \quad \Omega \equiv \frac{P_{2i}}{P_{1i}}; \quad \phi \equiv \frac{V_1}{V_2}; \quad t^* \equiv \frac{CP_{1i}}{2V_1}t; \quad C \equiv \frac{A_c^2}{\epsilon 8\pi\mu l_c};$$

where μ here is the N_2 gas dynamic viscosity and $\varepsilon \gtrsim 1$ is an empirical coefficient that accounts for additional bubble valve resistance. Refer to Fig. 10 for additional notation. The visco-inertial time scale in the cannula is $t_\mu \lesssim \rho R_c^2/\mu \approx 0.006$ s, where $R_c = 0.3$ mm and $\rho = 1.224$ kg/m^3 and $\mu = 18 \cdot 10^{-6}$ kg/m s for N_2 at 30 °C—much smaller than the average duty cycle of the bubble valve C2 $d = 0.05$ s, and significantly lower than the largest value of $d = 0.21$ s. Thus, the gas flow is dominated by viscous resistance in the cannula and may be approximated therein as this quasi-steady fully-developed viscous flow model with decreasing accuracy for decreasing d. Solution to Eq. (13) yields

$$P_1^* = j\left(\frac{1+k\exp[-2jt^*]}{1+\phi-(1-\phi)k\exp[-2jt^*]}\right), \tag{15}$$

from which the dimensional cannula exit volumetric flow rate may be determined

$$Q_2 \equiv Q_{gtheo} = CP_{1i}\frac{\left(P_1^{*2}-P_2^{*2}\right)}{2P_2^*}. \tag{16}$$

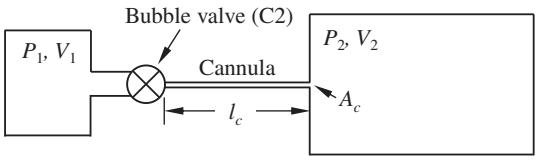

Fig. 10. Model of ideal viscous gas delivery through the cannula, where valve actuation is considered instantaneous. P and V refer to pressure and volume, respectively. A_c is the cannula cross section area and l_c is the cannula length.

For the experiments reported herein: $\phi \lesssim 0.2$ and $\Omega \approx 0.93$, and for such characteristic values, for small time $t^* \ll 1$, Eq. (16) is used to help establish the zeroth order correlation

$$Q_g = V_b f \approx (Q_2 d) f, \tag{17}$$

where f (Hz) is the bubble injection frequency through valve C2. Sequential measurements of spherical bubbles for a variety of pressures P_{1i}, volumes V_1, and duty cycles $d > 0.005$ s establishes $V_b \approx 4.0 \cdot d + 0.012$ (ml) with a 0.996 goodness of fit in Eq. (17). A flow resistance coefficient of $\varepsilon \approx 1.6$ equates experimental and analytical forms in Eq. (17). Eq. (17) thus provides a means for which to compute the gas flow rate given C2 valve duty cycle and frequency for the fixed volume gas delivery approach.

Via remote commanding, passive bubble separation tests employing the constant volume method of bubble injection could be conducted in approximately 2 min and over 2000 data sets are represented in this paper. Among other housekeeping measures, each data set includes the system values for the pump setting, liquid flow rate, slider location, C2 valve frequency and duty cycle, K3 piston position, and time dependent gas supply pressure in K3. Two of four video files are also available for each run: (1) Full image sequences using the High Speed High Resolution (HSHR raw) Motion BLITZ Cube 26H camera from Mikrotron, which can record up to 250 fps at a resolution of 1280 × 1024 px per frame camera, (2) processed HSHR video to improve telemetry efficiency, (3) a Hitachi HV-C20 MSG camera (MSG-1, 12 mm lens) for general surveillance, and (4) a second Hitachi MSG camera (MSG-2, 6 mm lens) for a more magnified view of the test section. The MSG camera sensors are 720 × 480 px at 30 fps.

The HSHR camera and Sill Optics Parallel Light Source (PLS) are the primary components of the Optical Diagnostics Unit (ODU) as shown in Figs. 6 and 8. The MSG cameras are shown in Fig. 6 positioned moderately askew to the optical axis of the HSHR camera. Sample images from these different devices are provided in Fig. 11. High image quality is provided by the HSHR camera, Fig. 11a. These 1.3 MB/frame images require substantial periods for downlink and are reserved for special test cases. Higher telemetry rates are achieved via onboard image processing as shown in Fig. 11b resulting in 0.16 MB/frame images that are wieldier for subsequent downlink to the ground in batch mode and are employed for highly quantitative data reduction without further optical corrections.

The MSG-2 image shown in Fig. 11c is clearly of lower quality to that of the HSHR camera due to lighting choices made to optimize the HSHR image, but this selectable MSG camera can be recorded on the ground in real time as low as approximately 8 fps.

Furthermore, by quantitatively comparing images of static bubble positions from both HSHR and MSG-2 camera images the lower resolution lower rate keystone images of the latter could be mapped onto the planar undistorted image plane of the former. This process is illustrated in Fig. 12, which shows a selection of approximately 80 known spherical bubble centroids that are used to construct a 3-dimensional scale factor field map via orthogonal regression to correct for distortions when the MSG-2 camera is employed. We determine that the MSG-2 images, despite moderate distortion and low resolution, can be used to effectively track bubble centroid locations for regime mapping with errors less than 3%. This level of uncertainly is acceptable to this end as it allows an order of magnitude increase in the amount of data collected and transmitted during the spaceflight experiments.

4.2. CCF experiments

A selection of MSG-2 camera images is provided in Fig. 13 suggesting the variety of phenomena to be discussed herein: In Fig. 13a a stable train of inscribed bubbles results if the bubble volume and frequency are small and the liquid flow rate is high. In Fig. 13b, if the bubble frequency is increased and/or the liquid flow rate is reduced, bubbles in the train can merge forming new bubbles large enough to migrate further, reach the free surface, coalesce, and escape the channel. In Fig. 13c, if the bubble volume is large and frequency is low, single bubbles do not leave the channel within the free surface length L if the liquid flow rate is over a threshold value. However, such bubbles would leave the flow through the free surface provided either the bubble injection location was further upstream, further away from the vertex, or the free surface was longer. In Fig. 13d the bubble volume, frequency, and liquid flow rate are such that 100% of the bubbles escape through the free surface within the channel length, $l < L$. The two-phase mass balance is simplified under such conditions as all gas entering the channel leaves within the field of view and the liquid flow rate is essentially the pump flow rate with estimated losses less than 3% due to splashing, leakage, and slight accumulation throughout the system due to transient pressure changes during the bubble injections. This is fortunate for our study making the 100% separation condition our most quantitative condition.

Experiments are conducted by varying channel length L (mm), liquid flow rate Q_l (ml/s), bubble volume V_b, and bubble frequency f. The latter two control variables effectively vary the gas flow rate Q_g (ml/s) and are controlled via gas supply valve duty cycle and actuation frequency, respectively. Bubble volumes in the range 0.004–2.14 ml are produced using this approach. A sample regime map is provided in Fig. 14a for a low, fixed bubble injection frequency of $f = 0.2$ Hz, where the state of the flow is identified as a function of Q_l and spherical bubble diameter $D_b = (6V_b/\pi)^{1/3}$ for fixed free surface length $L = 48$ mm. A subjective scale is applied to all intermediate conditions, but the demarcation between complete and partial separation is clear as identified in Fig. 14b, where only such points are shown. Thus, only bubble diameters that leave the channel within the channel length L for the specified liquid flow rate are shown in Fig. 14b. From the regime boundary curve, for fixed Q_l any increase in D_b is nearly certain to achieve 100% bubble separation in the channel. This data is collected at the lowest gas bubble frequency $f = 0.2$ Hz achievable which assures negligible bubble-to-bubble interaction. Only single non-merging bubbles larger than $D_{bmin} = 7.2$ mm ($V_{bmin} = 0.2$ ml) are certain to escape by capillary migration. However, bubbles with diameters as low as 6 mm can be observed to escape through the free surface at zero-to-low liquid flow rates. It is a point of this investigation to predict if there is sufficient channel length for escape of bubble diameters >7.2 mm for prescribed liquid flow rates—with and without bubble mergers. Again, only data for the full channel length $L = 48$ mm will be reported here.

Addressing conditions where bubble interactions are significant, the breadth of data presented is collected using regime maps that hold bubble frequency f constant while varying bubble volume V_b and liquid flow rate Q_l. The gas flow rate is in turn determined by $Q_g = f \cdot V_b$, and since the minimum single bubble escape volume

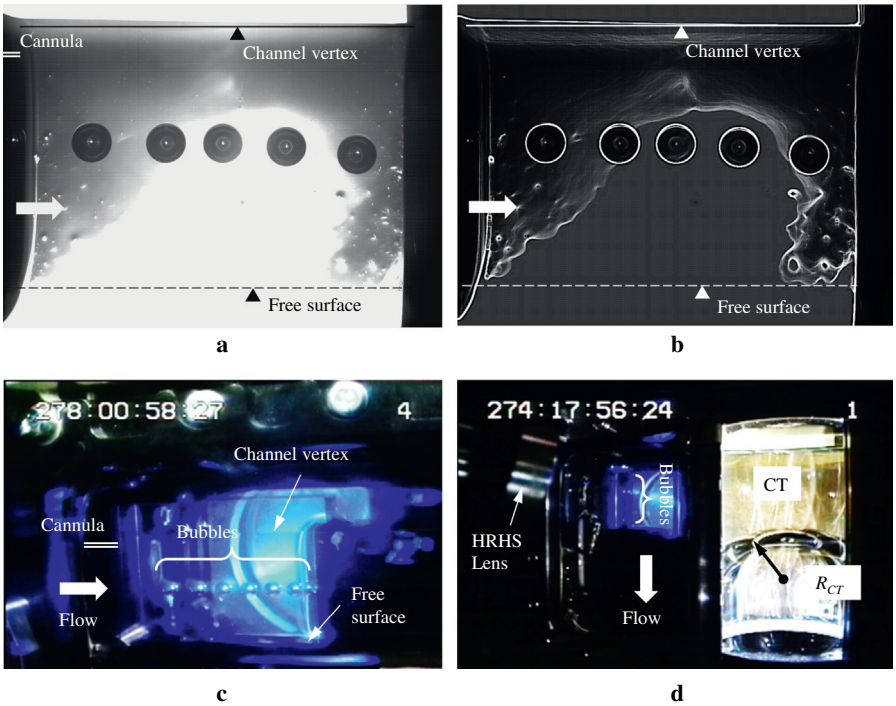

Fig. 11. Various annotated camera images and Fields of View: (a) HSHR (raw), (b) HSHR (processed), (c) MSG-2 (12 mm lens), and (d) MSG-1 (6 mm lens) (refer to Fig. 8). Flow direction is left to right except in (d), where flow is top to bottom. In d. the HSHR camera lens, capillary pressure regulator and reservoir (CT, refer to Fig. 9), and spherical cap meniscus are identified. Thin liquid films on the test channel exterior are visible in (a) and (b), but do not interfere with measurements.

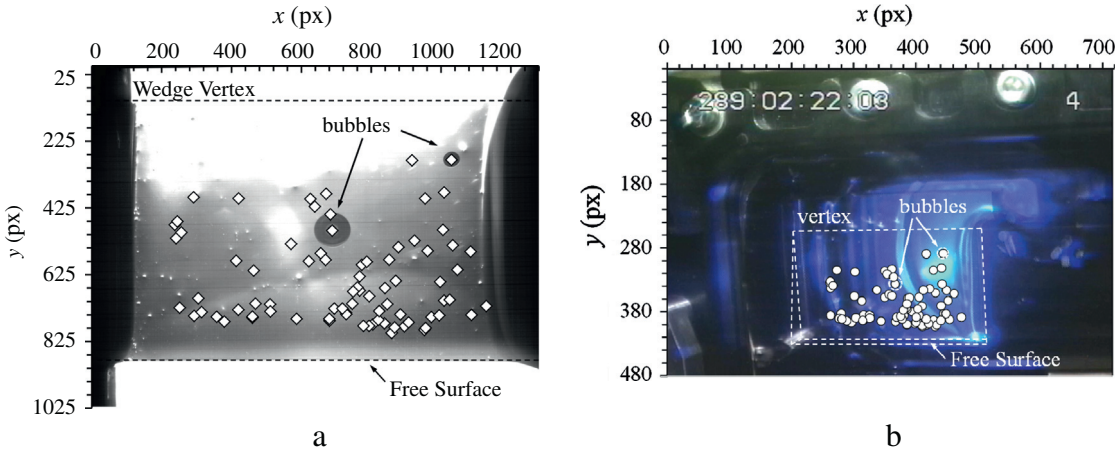

Fig. 12. Mapping of MSG-2 image to undistorted HSHR (raw) image. (a) HSHR image with two stationary bubbles. The bubble centroid is compared to that of the identical bubble in the MSG-2 camera view of (b) The diamond symbols in (a) identify the bubble centroids of similar tests used in the mapping. These points also appear as circle symbols in (b). The transform developed to map the MSG-2 positions in (b) to those of the HSHR camera in (a) establishes position uncertainties on average <3%.

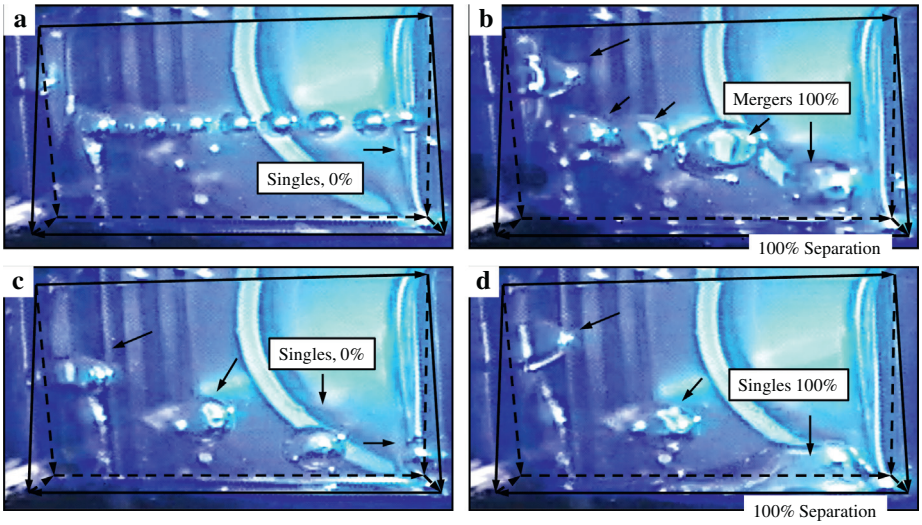

Fig. 13. Selection of CCF EU2 bubble separation phenomena for fixed Q_l = 1.75 ml/s: (a) non-separating low volume single bubble trains (d = 0.01 s, f = 2 Hz, V_b = 0.264 ml; File 2011-10-15-15h01m59s), (b) high frequency bubbles that merge with each other and then coalesce with the free surface a distance $l \leqslant L$ downstream (d = 0.05 s, f = 4 Hz, V_b = 1.25 ml; File 2011-10-03-22h06m29s), (c) large volume single bubbles that do not reach free surface within distance L downstream (d = 0.048 s, f = 1.5 Hz, V_b = 1.21 ml; 2011-10-16-15h08m57s), and (d) larger volume single bubbles that coalesce with the free surface a distance $l \leqslant L$ downstream (d = 0.6 s, f = 1.5 Hz, V_b = 1.46 ml; 2011-10-16-15h05m12s).

V_{bmin} is known, $Q_{gmin} = f{\cdot}V_{bmin}$. The extremes of outcomes for the fixed test cell dimensions are either when all bubbles remain in the test channel, 0% separation, or all bubbles leave the test channel, 100% separation. But many mixed modes are observed where any number of bubbles might remain or leave the channel. A typical experimental run fixes all parameters except the solenoid C2 duty cycle which is incremented or decremented until the point of complete phase separation is found. Four datasets are provided in Fig. 15. The 0% separation state is identified by open symbols and the 100% separation state is identified by solid symbols. Single bubble states are identified by black symbols and merged bubble states by red[1] symbols. Approximately 250 data points are required to construct each map and only completed maps are shown in Fig. 15 for f = 0.2, 0.5, 1, and 2 Hz with others to be finished during subsequent operations of the experiment on ISS. Significant data was also collected for bubble injection frequencies f = 0.1, 1.5, 3, 4, and 6 Hz. The maps become more complex as f increases due to bubble-to-bubble interactions, mergers, and turbulence as illustrated in Fig. 15d for f = 2.0 Hz.

Experimental data identifying the limits of complete separation are provided in Fig. 16 for the special case of bubble valve C2 held open and piston K3 moved at steady speeds with the gas flow rate determined by the piston travel rate. These tests are conducted by choosing a large value for the duty cycle (i.e., d = 10 s) and recording the bubble behavior. During the gas flow, upstream pressure differentials remain nominally above the 68 mbar threshold enabling loose comparisons with the constant volume tests. Bubble volumes are determined not by valve actuations but by the wedge geometry and liquid drag and shear forces. Nearly all bubbles merge prior to coalescing with the free surface and leaving the flow.

5. Discussion

In general, along the 100% separation boundary, the gas flow rate $Q_g = f{\cdot}Vb$ increases with liquid flow rate Q_l because larger bubbles are able to migrate toward the free surface in the shorter time available in part because they have a shorter distance to travel. Local plateaus in the Q_g versus Q_l behavior are observed in the

[1] (For interpretation of the references to colour in this figure legend, the reader is referred to the web version of this article.)

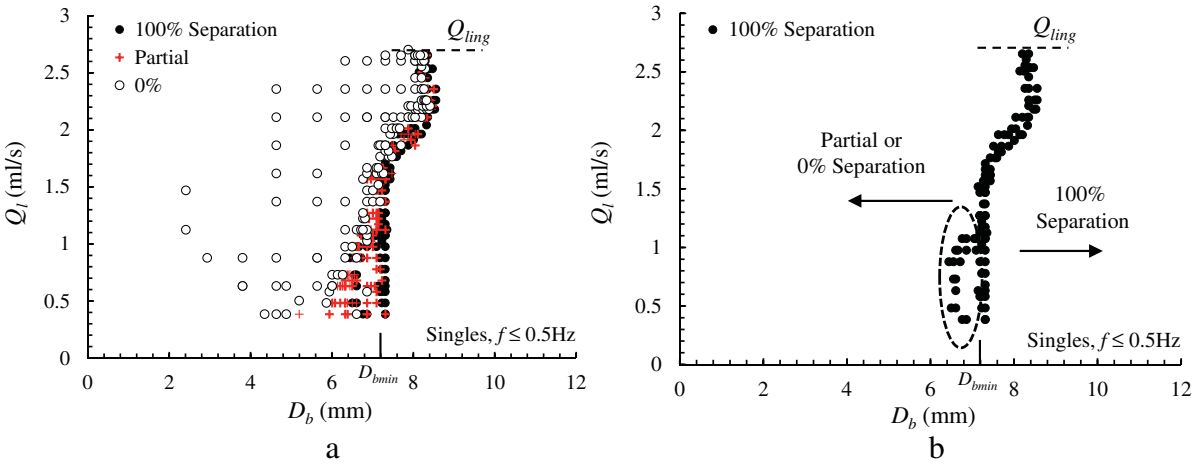

Fig. 14. Bubble diameters D_b that completely separate given the liquid flow rate Q_l: (a) A complete dataset where open circles identify 0% separation, red + signs partial separation, and black solid circles complete separation, (b) 100% separation data from (a), where complete separation is certain for all states right of the undulating curve. 100% separation conditions are identified by the dashed oval region where $D_b < D_{bmin} = 7.2$ mm and the inertial-capillary overshoot phenomenon propels the bubbles beyond their ideally inscribed elevations into and through the free surface. The ingestion limit $Q_{ling} = 2.69$ ml/s is identified by the dashed line. (For interpretation of the references to colour in this figure legend, the reader is referred to the web version of this article.)

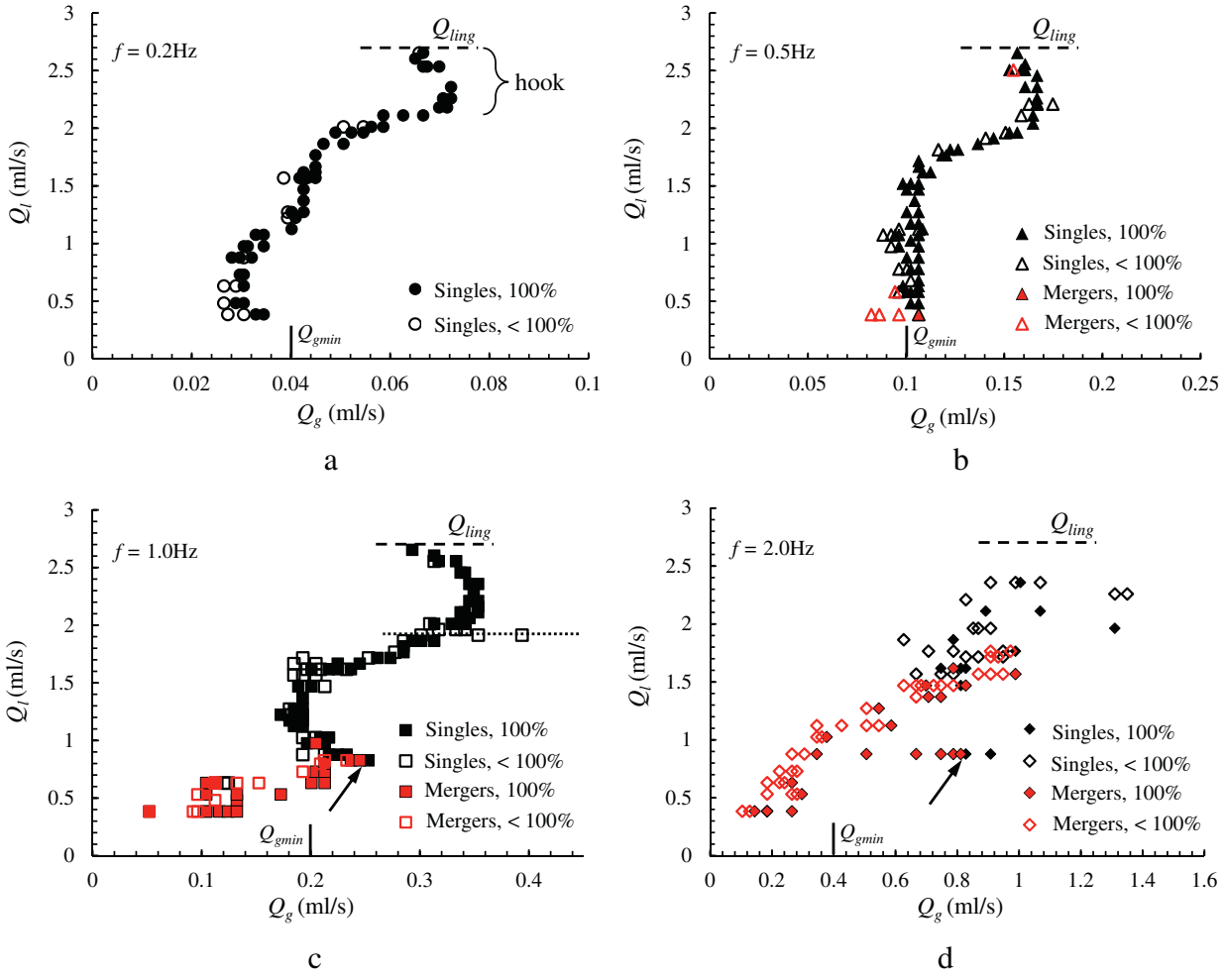

Fig. 15. Flow rate conditions for 100% bubble separation within an open wedge channel with half-angle $\alpha = 7.9°$, height $H = 30$ mm, and free surface length $L = 48$ mm: (a). bubble frequency $f = 0.2$ Hz single bubbles, (b) $f = 0.5$ Hz mostly single bubbles, (c) $f = 1$ Hz mixed single bubbles and bubble mergers, and (d) $f = 2$ Hz mostly mergers. All conditions right of the curves are expected to achieve 100% bubble separation within open wedge conduit length $l \leqslant 48$ mm. Cases identified with <100% separation pass at least one bubble out of at least six bubbles.

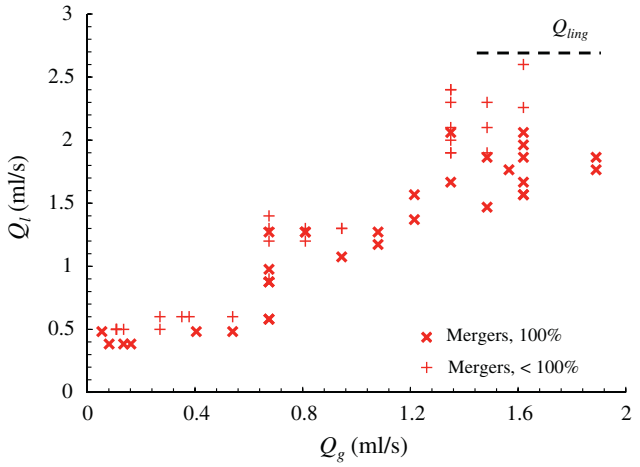

Fig. 16. 100% Bubble merger separation regime map for gas injection method where bubble valve C2 is held full open. Bubble volumes in this case are in part dependent on shear forces of the free stream velocity. Mergers and multi-mergers ensure bubbles of sufficient volume to coalesce with the free surface.

Fig. 15a–c curves. Despite the ragged appearance of the 100% separation conditions, the data is highly repeatable with changes in Q_g of less than 4% identifying boundaries between complete and partial separation. 'Near 100%' separations are identified for both single and merged bubble conditions that reveal how abrupt the regime transition is defined by the experimental method.

In Figs. 14b and 15a–c 100% separation conditions are observed for bubble volumes smaller than the minimum inscribed bubble volume in the range $0.137 < V_b < V_{bmin} = 0.20$ ml identified by the dashed oval region where $6.4 < D_b < D_{bmin} = 7.2$ mm. Such separations are possible due to the inertial-capillary overshoot phenomenon that can propel the bubbles beyond their ideally inscribed elevations into and through the free surface (Fig. 4). The phenomenon is suppressed with increases in Q_l.

As Q_g increases due to increases in f, for low Q_l, bubble mergers produce bubbles of sufficient size to successfully migrate out of the channel as identified in Fig. 15 using red symbols. The plots form curves where when Q_l is fixed, decreases in Q_g lead to bubbles that remain in the flow while increases in Q_g simply lead to more gas completely separating from the flow—albeit with increasing violence. Similarly, but conversely, for fixed Q_g, decreases in Q_l lead to only more certain bubble separation while increases in Q_l lead to partial and finally no bubble escape until Q_{ling} is reached.

The nature of the Q_l versus Q_g relationship can depend on bubble and wedge channel free surface natural frequencies. This is typified in Fig. 15c where at $Q_l \approx 1.9$ ml/s the 100% separation condition could not be achieved for any value of Q_g. In this case traveling capillary waves along the channel free surface match bubble injection frequencies at least inhibiting if not preventing coalescence. An obvious inflection in the data of Figs. 15a-c is apparent beginning at $Q_l \approx 1.8$ ml/s. Precise explanations for such behavior require further study, but at present we conjecture that such inflections are due to inward deflection of the free surface as bubbles coalesce with it, further enhancing contact, coalescence, and separation.

As Q_l approaches the ingestion limit $Q_{ling} = 2.69$ ml/s the free surface deflects up to approximately 7 mm into the 30 mm tall channel effectively shortening the bubble migration distance required to impact and coalesce with the free surface. This produces the hook observed in the Q_l versus Q_g curves near the Q_{ling} limit (refer Fig. 15a–c). For the case of Fig. 15d, local turbulence caused by numerous bubble mergers blurs the regime boundary. It is also observed from such tests that above the 100% separation condition the merged bubble regime can give way to the single bubble regime as Q_g is increased by increasing V_b, as shown in Fig. 15d with $Q_l \approx 0.85$ ml/s (see arrows in Fig. 15c and d).

For L fixed, the data of Figs. 15 and 16 are overlaid in Fig. 17 for only 100% separation conditions. Presented in this manner, it appears that the 100% separation condition is relatively weakly dependent on Q_l until bubble mergers become dominant for f between 1 and 2 Hz. For conditions $f \leqslant 0.5$ Hz in Fig. 17a the separations are free of bubble mergers though it is expected in all cases for small bubbles that mergers dominate the separation behavior as Q_l approaches 0. Our data is limited to $Q_l = 0$ and $0.38 \leqslant Q_l \leqslant 2.69$ ml/s.

For conditions $f = 0.2$ Hz and $L = 48$ mm, the bubble escape length l_H is plotted in Fig. 18 as a function of liquid flow rate Q_l for the data of Fig. 14b. With $Su^+ \gg 1$, $l_H \sim Q_l/(U_b H \tan\alpha)$, which is quantified in Table 1 under these conditions and calculated for each of the experimental points represented on the figure. The $O(1)$ fit coefficient does well to describe the trend, but a breakdown in the predictions is observed at the approximate location of the inflection point in the 100% separation curve of Fig. 14b, $Q_l \approx 1.75$ ml/s. Larger bubble volumes are required to escape within the free surface length $L = 48$ mm above this flow rate. As mentioned above, these bubbles have shorter distances to travel to reach the free surface, the latter which is also deflected further into the channel due to the approaching ingestion limit Q_{ling}. For these 100% bubble separation states, the x-component migration

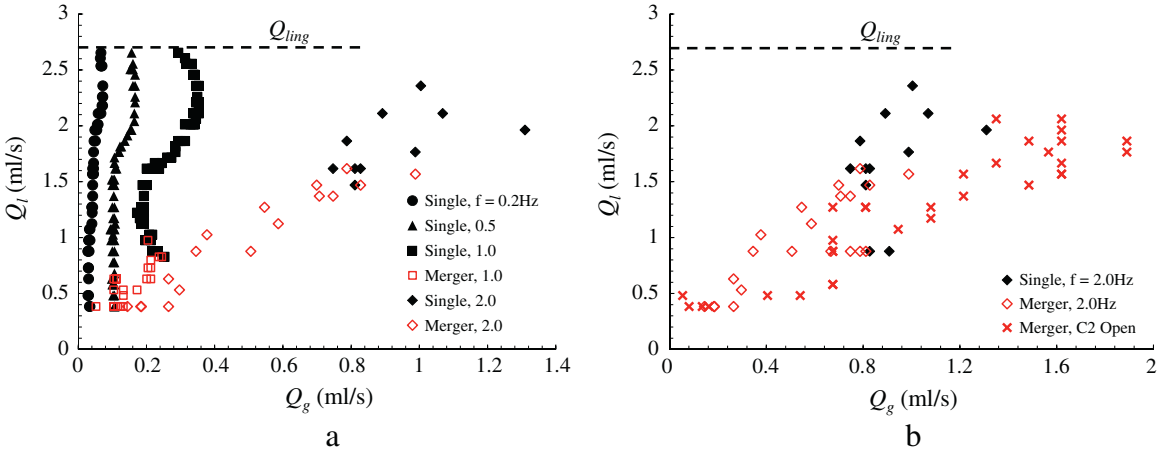

Fig. 17. (a) Overlay of 100% separation conditions of Fig. 15. (b) Overlay of 100% separation conditions of Figs. 15d and 16, where the $f = 2$ Hz data is seen to approach that of a wide open C2 valve.

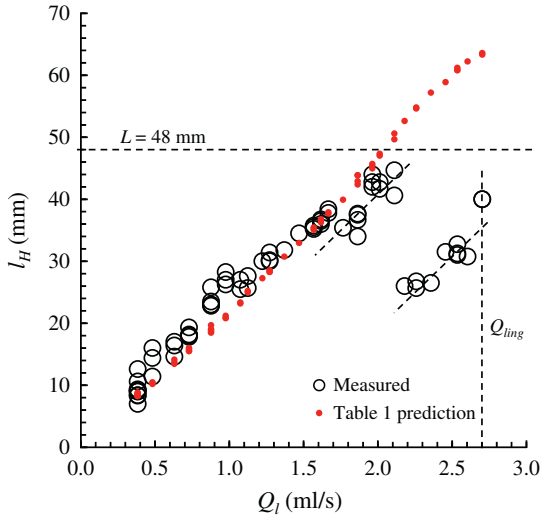

Fig. 18. Bubble/free surface escape length l_H as a function of liquid flow rate for f = 0.2 Hz, L = 48 mm. The size of the open black circles is a measure of experimental uncertainty. Small solid red circles provide results from predictions of l_H from Table 1 for each experimental data point. The maximum free surface length L and Q_{linq} = 2.69 ml/s are identified. The slopes appear similar for the non-conforming points as indicated by the dashed line segments. (For interpretation of the references to colour in this figure legend, the reader is referred to the web version of this article.)

velocity is approximately constant as shown in Fig. 4b, which is used to determine the 0.334 fit coefficient in Table 1 to find $U_b \approx 37.5 \pm 1.5$ mm/s for $0.14 \leqslant V_b \leqslant 0.328$ ml for the 68 data points represented in Fig. 18. This coefficient alone should be adequate to predict l_H, but coalescence of the bubbles with the free surface requires thinning films prior to rupture which apparently delays the coalescence and escape phenomena by approximately a factor of 3.51. This factor is required for the level of agreement observed in Fig. 18—the slope of the line may be repeated for the nonconforming data above ~2 ml/s.

Data reduction efforts are continuing on the large data set which is expected to be made publically available on the internet. Additional supplementary and complimentary investigations are pending, such as the impact of bubble frequency on U_b and l_H. Studies concerning turbulent transitions, developing boundary layers, the impact of longitudinal free surface waves arising from natural frequencies and bubble coalescence frequencies, Magnus effects, Saffman lift, bubble merge phenomena, droplet ejections during coalescence, and others are readily conducted using the video archive collected during the CCF ISS experiments and now serving as a database. Numerical and theoretical methods can proceed with a wealth of supporting data for benchmarking as is and will continue to be pursued in subsequent work.

6. Summary

It is clear that the wedge conduit geometry serves well as a passive bubble phase separating device. For a broad range of flow conditions, bubbles within the flow are driven away from the conduit vertex by capillary forces. Depending on the gas and liquid flow rates, characteristic bubble volumes, and vertex included angle, the migrating bubbles collect and merge in the widest region of the conduit section. If a free surface is present, as in the case of the CCF experiments performed aboard the ISS, the merged bubbles may escape through the liquid free surface achieving a desirable 100% passive separation function. The following considerations can serve to guide the design process when exploiting laminar flow along acute polygonal conduits such as the open asymmetric wedge channel of this investigation:

1. Bubble volumes V_b with spherical bubble diameters D_b smaller than the maximum inscribed circle diameter of the wedge section D_{bmin} (or V_{bmin}) are unlikely to contact the free surface, $V_b < (4\pi/3)(H\sin\alpha/(1+\sin\alpha))^3$. Such bubbles do not exit the flow, but rather migrate to certain elevations from the conduit vertex $\sim D_b/2\sin\alpha$ and are convected more or less linearly downstream (Fig. 13a and c). In general, these bubbles tend to travel at approximately inscribed elevations.
2. At low $Q_l \sim Q_{gmin} = f\ V_{bmin}$, a range of bubbles with volumes smaller than V_{bmin} can exit the free surface due to inertial-capillary effects. In such cases the capillarity-driven bubble migration creates wake vortices that propel the bubbles beyond their ideally inscribed elevations and into and through the free surface.
3. When $V_b > V_{bmin}$ all bubbles will eventually separate provided Q_l is low enough and the channel length L is long enough—the 100% separation condition. For the inertial-capillary bubble migration conditions presented herein, separations occur when $l_H \approx 10.5(Q_l/H)(\rho V_b^{1/3}/2\sigma\tan^{4/3}\alpha)^{1/2} < L$; the time for the bubble to migrate across the channel height H is approximately 3.5 times shorter than the time to convect along the channel length L.
4. For small bubble volumes at high gas flow rates Q_g (i.e., high bubble injection frequency f), provided Q_l is low enough, bubble mergers readily increase bubble volumes to the point of 100% separation (Figs. 13b, 15c and d).
5. Characteristic bubble migration velocities are identified for both viscous- and inertia-dominated conditions (Eqs. (2)–(4)). Further details of the viscous regime are addressed by Reyssat (2014). As a zeroth order approximation, such velocities may be superposed onto a known velocity profile caused by the forced liquid flow through the duct to construct bubble trajectories from which the conduit length l_H for 100% separation may be estimated (Table 1).

The 100% phase separation maps of Fig. 15 may be used in conjunction with the semi-quantitative scale quantities of Table 1 to determine the necessary channel dimensions to achieve 100% separation for required or specified flow rate ranges and ratios. Such tools are useful for engineering designs with applications in macro-scale systems aboard orbiting spacecraft as well as micro-scale systems on Earth. Concerning the CCF ISS experiments, further experiments have been conducted and are being planned. Reduction efforts are continuing on the large data set which is expected to be made publically available on the internet. Numerical and theoretical methods can proceed with a wealth of supporting data for benchmarking.

Acknowledgements

Support for this work is shared by the National Aeronautics and Space Agency cooperative agreement NNX09AP66A and the German Federal Ministry of Economics and Technology (BMWi) via the German Aerospace Center (DLR) under Grant No. 50WM1145. We wish to thank astronaut Mike Fossum, PSU graduate student Will Blackmore, Astrium Engineering, and the NASA cadre at Glenn Research Center, Johnson Space Center, and especially the MSG crew at Marshall Spaceflight Center for support during the flight operations. A.P. Wollman is supported in part through NASA/Oregon Space Grant Consortium grant NNX10AK68H.

Appendix A

For the experimental results presented herein, Tables A1 and A2 provide maximum values for certain dimensionless groups and the

Table A1
Representative maximum values of experimentally determined dimensionless groups of this investigation. Microgravity conditions are $g \sim 10^{-6} g_o$ on ISS and $g \leqslant 10^{-4} g_o$ in the drop tower (DT), where $g_o = 9.81\ m/s^2$. In this table the characteristic length $R = 0.4$ cm is the maximum half-width of the CCF channel and maximum measured capillary and forced flow velocities for HFE-7500 are approximately 4.5 and 3.0 cm/s, respectively. The maximum capillary velocities for the 10 and 50 cSt drop tower tests are 4 mm/s and 2 mm/s, respectively. ($Su^+ \equiv Su\cdot((3/4\pi)\tan^8\alpha)^{1/3}$ with $\alpha_{ISS} = 7.9°$ and $\alpha_{DT} = 7.75°$.)

Parameter	HFE-7500 ISS	HFE-7500 DT	10 cSt PDMS DT	50 cSt PDMS DT
Bo	$1.6(10^{-4})$	$1.6(10^{-3})$	$7.3(10^{-4})$	$7.5(10^{-4})$
Re_{cap}	242	242	1.6	0.16
Re_{forced}	161	–	–	–
We_{cap}	0.81	0.81	$3.0(10^{-3})$	$7.4(10^{-4})$
We_{forced}	0.36	–	–	–
Su	$6.7(10^4)$	$6.7(10^4)$	860	33
Su^+	214	203	2.6	0.11

Table A2
Nominal fluid properties at 25 °C with surface tensions with air assumed (1100 mbar).

Fluid	ρ (kg/m^3)	μ (10^{-3} kg/m s)	σ (10^{-3} kg/s^2)
Novec HFE-7500	1614	1.25	16.2
PDMS, 5 cSt	913	4.56	19.7
PDMS, 10 cSt	927	9.27	20.1
PDMS, 50 cSt	960	48.0	20.8
Nitrogen, N_2	1.24	0.018	–

nominal thermophysical properties used to compute them, respectively. Inertial forces are compared to surface tension forces invoking the Weber number $We = \rho U^2 R/\sigma$, where U characterizes the free stream velocity normal to the interface and μ is the dynamic viscosity of the liquid. The Reynolds number is $Re = \rho UR/\mu$. As gathered from Table A1, the flows studied are laminar ($Re \leqslant 200$) and dominated by surface tension ($Bo \ll 1$) with expectations of significant interface deflections and possible instability due to non-negligible inertia at free surfaces ($We \leqslant 0.81$).

References

Barbu, A., Ellis, M., Kurwitz, C., Best, F., 2006. Acoustic gauge monitoring of fluid inventory in a microgravity vortex separator. Meas. Sci. Technol. 17, 403–410.

Canfield, P.J., Bronowicki, P.M., Chen, Y., Kiewidt, L., Grah, A., Klatte, J., Jenson, R., Blackmore, W., Weislogel, M.M., Dreyer, M.E., 2013. The capillary channel flow experiments on the International Space Station: experiment setup and first results. Exp. Fluids 54, 1519.

Chahine, G.L., Kalumuck, K.M., 2001. Swirling Fluid Jet Cavitation Method and System for Efficient Decontamination of Liquids, US Patent 6,221,260, April 24.

Chato, D.J., Martin, T.A., 2006. Vented tank resupply experiment: flight test results. AIAA J. Spacecraft Rockets 3 (5).

Clark, W.D., 1992. Zero Gravity Phase Separator Technologies—Past Present and Future, ICES, 921160, Seattle, July 13–16.

Concus, P., 1964. Capillary stability in an inverted rectangular channel for free surfaces with curvature of changing sign. AIAA J. 2 (12), 2228–2230.

Concus, P., Finn, R., 1969. On the behavior of a capillary free surface in a wedge. Proc. Natl. Acad. Sci. USA 63 (2), 292–299.

Feng, Y., Seyed-Yagoobi, J., 2004. Control of liquid flow distribution utilizing EHD conduction pumping mechanism. 39th IAS Annual Meeting, Industry Applications Conference, vol. 4. IEEE, Seattle, WA.

Hoyt, N., Kang, M.F., Kharraz, A., Kadambi, J., Kamotani, Y., 2011. Cyclonic two-phase flow separator experimentation and simulation for use in a microgravity environment. J. Phys.: Conf. Ser. 327.

Jaekle Jr., D.E., 1991. Propellant management device conceptual design and analysis: vanes. In: 27th AIAA/SAE/ASME/ASEE Joint Propulsion Conf., AIAA-91-2172, August, Sacramento.

Klatte, J., 2011. Capillary flow and collapse in wedge-shaped channels (Ph.D. thesis), Universität Bremen.

Klatte, J., Haake, D., Weislogel, M.M., Dreyer, M.E., 2008. A fast numerical procedure for steady capillary flow in open channels. Acta Mech. 201 (1–4), 269–276.

Ku, J., 1999. Operating characteristics of loop heat pipes. In: 29th Int. Conf. On Environmental Systems, 1999-01-2007, July 12–15, Denver, CO.

Marchetta, J., Winter, A., Hochstein, J., 2004. Simulation and prediction of realistic magnetic positive positioning for space based fluid management systems, AIAA-2004-1151. In: 42nd AIAA Aerospace Sciences Meeting and Exhibit, Reno, Nevada, 5–8 January.

Melin, J., van der Wijngaart, W., Stemme, G., 2005. Behaviour and design considerations for continuous flow closed-open-closed liquid microchannels. Lab on a Chip, First Published as an Advance Article Online, 21st April, doi: http://dx.doi.org/10.1039/b501781e.

Metz, T., Paust, N., Zengerle, R., Koltay, P., 2010. Capillary driven movement of gas bubbles in tapered structures. Microfluid. Nanofluid. 9, 341–355. http://dx.doi.org/10.1007/s10404-009-0551-1.

Oeftering, R.C., Chato, D.J., Mann III, A., 2002. Liquid Propellant Manipulated Acoustically, Research and Technology 2002, NASA/TM-2003-211990.

Orlando, R., Ferrara, M., 1992. Effects of Air Bubble Contamination in Recirculating Water Loop, SAE Technical Paper 921282, doi: http://dx.doi.org/10.4271/921282.

Ozbolt, T.A., 1996. US lab architecture control document, volume 7: temperature and humidity control, revision new, D683-14719-1-7. Boeing Defense and Space Group, Missile & Space Division, Huntsville, Alabama, December 20, 1996 (Hamilton Sundstrand).

Pettit, D.R., M.M. Weislogel, Concus, P., Finn, R., 2011. Beverage Cup for Drinking Use in Spacecraft or Weightless Environments, NASA, US Patent. No. 8,074,827, December 13.

Reyssat, E., 2014. Drops and bubbles in wedges. J. Fluid Mech. 748, 641–662.

Rosendahl, U., Dreyer, M.E., 2007. Design and performance of an experiment for the investigation of open capillary channel flows. Exp. Fluids 42 (5), 683–696.

Rosendahl, U., Ohlhoff, A., Dreyer, M.E., 2004. Choked flows in open capillary channels: theory, experiment and computations. J. Fluid Mech. 518, 187–214.

Shoemaker, J.M., Schrage, D.S., 1997. Microgravity fluid separation physics – experimental and analytical results. In: 35th Aerospace Sciences Meeting & Exhibit, Aerospace Design and Fabrication, AIAA-97-0886, Reno, NV, January 6–9.

Skelleya, A.M., Voldmana, J., 2008. An active bubble trap and debubbler for microfluidic systems, Lab on a Chip, First Published as an Advance Article Online, 28th August 2008, doi: http://dx.doi.org/10.1039/b807037g.

Spivey, R.A., Sheredy, W.A., Flores, G., 2008. An overview of the Microgravity Science Glovebox (MSG) facility, and the gravity-dependent phenomena research performed in the MSG on the International Space Station (ISS). In: 46th AIAA Aerospace Sciences Meeting, AIAA-2008-0812.

Thurman, R., McCall, F., 1992. Design and Control of Space Station Freedom U.S. Laboratory Active Thermal Control System, SAE Technical Paper 921109, doi: http://dx.doi.org/10.4271/921109.

Weislogel, M.M., Lichter, S., 1998. Capillary flow in interior corners. J. Fluid Mech. 373, 349–378.

Weislogel, M.M., Thomas, E.A., Graf, J.C., 2009. A novel device addressing design challenges for passive fluid phase separations aboard spacecraft. J. Microgravity Sci. Technol. 21 (3), 257–268.

Weislogel, M.M., Baker, J.A., Jenson, R.M., 2011. Quasi-steady capillary-driven flows in slender containers with interior edges. J. Fluid Mech. 685, 271–305.

Wollman, A., 2012. Capillarity-driven droplet ejection. Master's thesis, Portland State University. Permanent Link: <http://archives.pdx.edu/ds/psu/8243>.

Xu, J., Vaillant, R., Attinger, D., 2010. Use of a porous membrane for gas bubble removal in microfluidic channels: physical mechanisms and design criteria. Microfluid Nanofluid, Published Online: 24 March, doi: <http://dx.doi.org/10.1007/s10404-010-0592-5>.

Zhao, B., Moore, J.S., Beebe, D.J., 2001. Surface-directed liquid flow inside microchannels. Science 291, 1023. http://dx.doi.org/10.1126/science.291.5506.1023.